Unclonable micro-texture with clonable micro-shape towards rapid, convenient, and low-cost fluorescent anti-counterfeiting labels

Yuhong Lin[1, #], Hongkun Zhang[2, #], Jingyun Feng[1, #], Bori Shi[1], Mengying Zhang[3], Yuexing Han[2, 4*], Weijia Wen[5], Tongyi Zhang[1], Yabing Qi[6] and Jinbo Wu[1*]

1 Materials Genome Institute, Shanghai University, Shanghai 200444, China. Email: jinbowu@t.shu.edu.cn

2 School of Computer Engineering and Science, Shanghai University, Shanghai 200444, China. Email: han_yx@i.shu.edu.cn

3 Department of Physics, Shanghai University, Shanghai 200444, China.

4 Shanghai Institute for Advanced Communication and Data Science, Shanghai University, Shanghai 200444, China

5 Department of Physics, The Hong Kong University of Science and Technology, Hong Kong, China.

6 Energy Materials and Surface Sciences Unit (EMSSU), Okinawa Institute of Science and Technology Graduate University (OIST), 1919-1 Tancha, Onna-son, Okinawa 904-0495, Japan

Keywords: anti-counterfeiting, physical unclonable function, perovskite, divide-and-conquer, evaporative assembly, laser engraving

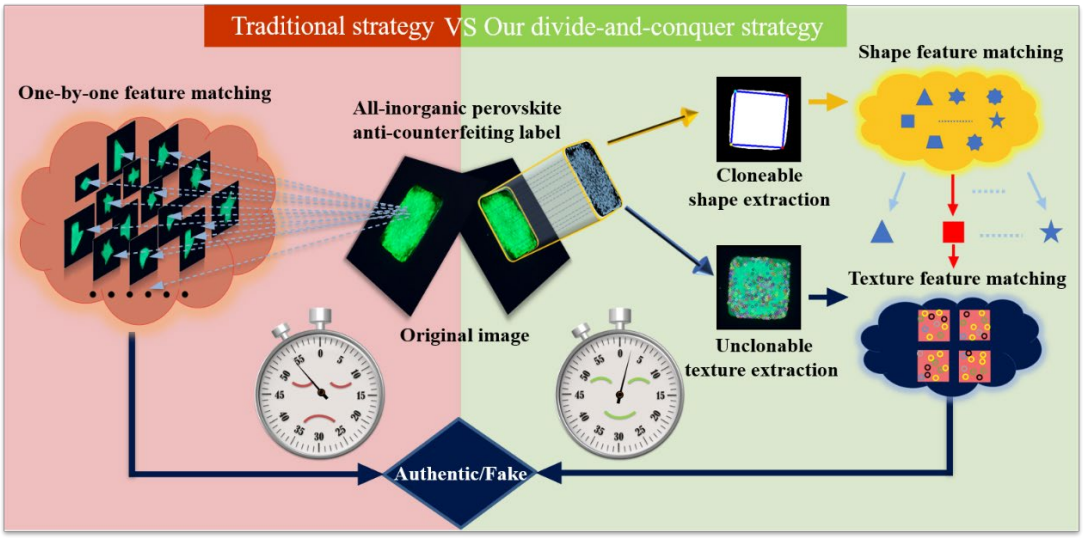

Abstract: An ideal anti-counterfeiting label not only needs to be unclonable and accurate, but also must consider cost and efficiency. But the traditional physical unclonable function (PUF) recognition technology must match all the images in a database one by one. The matching time increases with the number of samples. Here, we introduce a new kind of PUF anti-counterfeiting label with high modifiability, low reagent cost (2.1×10^{-4} USD), simple and fast authentication (overall time 12.17s), high encoding capacity (2.1×10^{623}), and its identification software. All inorganic perovskite nanocrystalline films with clonable micro-profile and unclonable micro-texture were prepared by laser engraving for lyophilic patterning, liquid strip sliding for high throughput droplet generation, and evaporative self-assembling for thin film deposition. A variety of crystal film profile shapes can be used as "specificator" for image recognition, and the verification time of recognition technology based on this divide-and-conquer strategy could be decreased by more than 20 times.

1. Introduction

Counterfeit products have long plagued societies across the globe. From high-end luxury goods to medical supplies, counterfeit products not only cause tremendous economic losses but also pose a massive threat to people's health. [1-3] Therefore, it is necessary to establish a safe and reliable anti-counterfeiting system consisting of cheap and reliable anti-counterfeiting labels and a convenient and fast authentication system. Unfortunately, many of the widely used anti-counterfeiting methods rely on clonable labels produced by a deterministic process. These labels are low-cost, but their simple

and repeatable preparation processes and regular decoding mechanisms are exploitable by counterfeiters. [4, 5] Many of the more complex and safer anti-counterfeiting labels (such as high-end RFID labels with large number of logic gates) cannot become standard on some commonly used products due to their high cost. [5, 6] Anti-counterfeiting labels with physical unclonable functions (PUF) are a feasible solution to the above shortcomings. Since the introduction of the PUF in 2002[7], many anti-counterfeiting labels with different PUF characteristics have been developed, such as unique bionic fingerprint pattern with random surface topography [8-10]; randomly distributed nanoparticle pattern, including flower-like patterns with random pinning points [11], nanowires coated with fluorescent dyes in random positions [12] etc. In addition, researchers have prepared many types of PUF anti-counterfeiting labels with optical response. For example, Cheng et al.[13] reported a multicolor plasma nanopaper with random Raman intensity distribution, He et al.[14] designed a multi-mode structural-color anti-counterfeiting labels composed of randomly arranged nanospheres, and Leem et al.[15] developed edible silk film labels with random light response. To improve the capabilities and speed of unclonable-pattern recognition, researchers further developed computer image processing and recognition techniques to complete the matching of unclonable patterns with the target patterns in database.

In the search for a better algorithm, Liu et al. [11] used the deep learning method for the first time to learn the features of a large number of unclonable patterns and then complete the verification of the unclonable patterns. The advantage of this method is that it uses neural network parameters to record the information of unclonable features so that the pattern verification can be completed only through the neural network, considerably improving the speed and accuracy. By training on images from different angles, the neural network can accurately and rapidly identify the patterns taken by different people and at different angles, but the model training is required for each new PUF pattern. Jing et al.[16] developed a deep learning (DL)-facilitated software to pre-categorize the hierarchical topographies with classifiable features, which can shorten the overall authentication time.

Conventional recognition techniques are based on feature points matching and

every time a new product is added, it is not necessary to modify the algorithm—only the database needs to be updated. For example, Takahashi et al. [17] used the Oriented FAST and rotated BRIEF (ORB) algorithm to extract the features of a macro image as ID tags, used a brute-force matcher to match the feature points with the saved image, and used random sample consensus to reduce the feature points, thus detecting the specific product serial number. Wigger et al.[18] also used the macro characteristics of a material at the time of preparation for image matching. Han et al.[19] proposed a computer vision technique that used the scale-invariant feature transform (SIFT) algorithm to select feature points and used a brute-force matcher to match feature points, an approach that showed good results. This technique enables the accurate verification of the security label without physical marking. Gu et al.[20] drop-cast a mixed solution of various gap-enhanced Raman tags (GERTs) on a silicon substrate and obtained a pattern of randomly distributed particles after drying. The PUF label was then read by performing Raman mapping with a resolution of different pixels using a confocal Raman system. The nonnegative least squares method was used to demultiplex the mixed spectra, and a global search algorithm and coarse-grained coding method were used to digitize the PUF tags with strong signal and high stability. Although these matching methods have showed excellent performance, they need to be matched with library files one by one, so the matching time may increase as the number of samples increase.

An ideal unclonable anti-counterfeiting technique must be inexpensive, mass-producible, nondestructive, and convenient for authentication. These requirements deny the use of complex and expensive reagents in the preparation of anti-counterfeiting labels and call for verification process simple and easy to operate. Photoluminescent nanomaterials have been widely used in the field of anti-counterfeit in recent years.[21, 22] Furthermore, perovskite materials are promising candidates for optical security labels with easy solution-processability, ionic crystal characteristic, and high fluorescent quantum yield.[10, 23] For example, by using $CsPbBr_3$ perovskite nanocrystals (NCs) as eikonogen , Li et al. designed and fabricated an individual Cloud based fingerprint operation platform to achieve high-definition latent fingerprint analysis. [24] Liu et al. proposed a facile strategy to fabricate an unclonable super micro fingerprint (SMFP) array by introducing in situ grown perovskite crystals for multilevel anticounterfeiting labels. [10] Yu et al. emonstrated the potential applications of hydrochromic $CsPbBr_3$ NCs in anti-counterfeiting by using $CsPbBr_3$

NCs@mesoporous silica nanospheres as the starting material. [25]In this paper, we introduce an unclonable anti-counterfeiting technique with high-throughput and low-cost preparation and convenient, rapid and repeatable verification. In our method, a nanosecond laser was used to engrave the lyophobic substrate, exposing the patterned lyophilic region. Then, by the sliding method, the preprepared $CsPbBr_3$ precursor solution was selectively and parallelly deposited on the patterned lyophilic region, and self-assembly was induced by heating and evaporation. The all-inorganic perovskite precursor solution confined on the lyophilic region evaporated and crystallized to form a nanocrystalline film with certain shapes or profiles. Due to the randomness of the crystallization process and the irregularity of the substrate after laser engraving, the formed crystal film has a unique micro-texture that exhibits PUF characteristics. Meanwhile, adjusting surface wettability can effectively control texture formation. [26-28] For hydrophobic substrates, in the case of the heated substrate, the suppression of the transition (from CCR to CCA mode) occurs and the contact line almost remains pinned during most of the time of the evaporation, forming a ring and an inner deposit. [28] For hydrophilic substrates, peripheral rings with uniform deposition in the center are observed, the latter due to thermal Marangoni effect. With heating of substrate, the rings become thinner as Marangoni effect becomes stronger. [26] The fluorescent images of the perovskite thin film were taken under ultraviolet (UV) light, and then the shape and texture information of the images were extracted by our self-developed ShatexMatch software. In anti-counterfeiting verification, the software first classified the shape of the pattern and then validated the texture, which greatly improved the efficiency of image recognition. The verification and matching time of a single image was shortened from 54.18 s to 2.69 s. End users just need a connected smartphone, a handheld microscope to complete the inspection, and no other professional equipment and skill is required. The overall processing time (smartphone readout + data synchronization + authentication) was only 12.17s by our ShatexMatch technology. For our anti-counterfeiting labels, each basic unit can be used as a “pixel” to form a macro graphic. They are highly modifiable from the basic unit to the two-dimensional macro pattern. Fluorescence acts as the simple first layer of anti-counterfeiting; the macro graphics composed of basic units can carry information (such as a two-dimensional code), which is used as the second layer of anti-counterfeiting; the basic micro units with different shapes are used as the third layer of anti-counterfeiting; the units with the same shape and unique texture serve as the fourth layer of anti-counterfeiting. The

verification process of a total of four layers of anti-counterfeiting can be completed on the end users. In short, the anti-counterfeiting label, we developed, demonstrating low reagent cost (2.1×10^{-4} USD), simple and fast authentication (12.17s), huge encoding capacity ($2.8\times10^{1,043}$) and high modifiability with four-layer verifications. These characteristics all show good commercial application prospects.

2. Results and discussion

2.1 Preparation of perovskite film arrays

2.1.1 Full lyophilic pattern

Figure 1 (a-d) depicts the process of preparing a patterned array of perovskite films by using our previous surface-tension-confined (STC) method. [29-31] The cleaned substrate was modified with 1*H*,1*H*,2*H*,2*H*-perfluorooctyltriethoxysilane (POTS) to prepare a lyophobic surface. A UV nanosecond laser was used to engrave the surface of the substrate to form a patterned lyophilic array on the surface of the substrate. The patterned lyophilic array on the lyophobic surface effectively guided the dewetting process. A small amount of liquid was split and confined onto the lyophilic surface, and tens of thousands of isolated droplets were formed by pinning the three-phase contact line (TCL) at the junction of the lyophilic/lyophobic region.

To predefine the pattern shape, we engraved the substrate with different laser powers. If the laser power was too low (such as 50 kHz, 1.4 W), the difference between the lyophilic and lyophobic regions of the substrate after engraving was not distinct, the TCL shrank when the precursor droplet evaporated, and the final formed array of crystal films had an irregular outer profile (Figure S1b2). If the laser power was too high (such as 50 kHz, 2.1 W), the thermal effect of the nanosecond laser destroyed the lyophobic layer outside the predefined pattern, forming a profile as shown in Figure S1d1. After the precursor droplet evaporated, the formed array was considerably larger than the predefined pattern and had irregular outer edges (Figure S1d2). Therefore, 50 kHz and 1.7 W were chosen as the processing parameters. At this time, the circular pattern of 150 μm was predefined, and the circle of 170 μm was obtained after the droplet evaporated (Figure S1c2).

As shown in Figure 1e1, the lyophilic pattern was engraved with a suitable laser power, and the surface profile is shown in Figure 1e2. The flat surface was engraved with ripples with a spacing of approximately 3 μm (Figure S2), and the surface roughness (arithmetic mean difference of the profile) was 12.9 nm. We found that when the temperature of the hot plate was 20°C, the droplets evaporated slowly (about 1h),

forming a small number of large and irregularly dispersed crystals (Figure 1h1, i1). When the temperature of the hot plate was increased to 40°C, due to the combined action of the surface capture effect (the rapid drop of the air-liquid surface of the droplet and the thermally driven Marangoni flow) and the coffee-ring effect [32, 33], the radial flow inside the droplet sent the solute particles to the edge of the droplet, where they accumulated. Meanwhile, the height of the droplet decreased, and the solute particles in the droplet became enriched at the gas–liquid interface of the droplet. Finally, the droplet evaporated, and a crystal film formed with two edges significantly higher than the center; the height difference between the highest edge and the average height reached 607 nm (Figure 1h2 and i2). When the temperature of the hot plate was 60°C, the droplets evaporated quickly (about 10s). The surface trapping effect became stronger, forming a crystal film with both edges slightly higher than the center, and the height difference between the highest edge of the crystal film and the average height reduced to be 139 nm. Compared with the film formed at 40°C, the film formed at 60°C was more uniform. As can be seen from Figure 1g1and g3, the crystal grains were more densely packed at the edges of the droplet. When the temperature of the hot plate continued to rise to 80°C, the height difference between the highest edge of the formed crystal film and the average height dropped to 127 nm. With a square as an example, we attempted to prepare crystal films of different sizes. The size gradient is shown in Figure S3. When the pattern size was as small as approximately 30 μm, the outer profile of the square film was distorted to a certain extent, so the size of the subsequent pattern preparation was equal or greater than 50 μm due to the limited processing accuracy.

Figure S4 shows the X-ray diffraction (XRD) characterization data of the resulting sample. The main diffraction peaks at 15.2° (110), 21.5° (112), and 30.7° (220) were all characteristic peaks of $CsPbBr_3$ crystals. Through statistical analysis of SEM images using ImageJ (Figure 1g1, g2), the average crystal-grain size was determined to be 239 nm. In addition, the fluorescence spectrum (Figure S5a) showed that $CsPbBr_3$ nanocrystals had an absorption peak at 514 nm, a photoluminescence (PL) peak at 520 nm, and a Stokes shift from 514 nm to 520 nm between emission and band-edge absorption. The full width at half maximum (FWHM) was approximately 17 nm, indicating that the size uniformity of the prepared $CsPbBr_3$ nanocrystals is high. Furthermore, it can be seen from Figure S5b that the short lifetime $\tau 1$ of the prepared $CsPbBr_3$ crystal was 2.19 ns, the long lifetime $\tau 2$ was 12.4 ns, the average lifetime was 10.42 ns, and the corresponding photoluminescence quantum yield (PLQY) was 3.11%.

2.1.2 Controlling the inner part of the pattern

In addition to the simple preparation of solid geometric figures, we attempted to prepare hollow patterns. We found that when the lyophilic pattern was a closed loop shape (Figure 2a), the surface trapping effect did not take effect every time (Figure 2c). When the air-liquid interface descends rapidly, it is possible that solute particles are enriched at the gas–liquid interface to form a fully covered film due to the surface trapping effect. When the air-liquid interface descends extremely low, the liquid film is very thin and unstable. Due to the disturbance of the lyophobic part[34], the liquid film may dewet or rupture with a certain probability, resulting in a loop-shaped or partially covered film. To ensure that the data were representative, we calculated the film formation rate of 72 samples. The statistical analysis showed that the probability of forming a fully covered film was approximately 46%, the probability of a partially covered film was 37%, and the probability of a loop was 17%.

We added a small gap of appropriate length to the loop pattern (Figure 2d), so that the coated precursor solution was distributed along the lyophilic region, instead of forming large droplets (Figure S6). Through experimental observation, we found that the smallest gap that yielded a liquid circle was 14 μm. Then a loop-shaped film with an average height of 62 nm was prepared, and the loop-shaped film also showed a high-edge and low-center distribution due to the coffee-ring effect (Figure 2e1, e2, g). In this way, we prepared the combined pattern of a loop and a solid pattern as shown in Figure 2l in one step.

To demonstrate the highly tunability and versatility of our technique, we used different pixel elements (such as stars, squares, and circles) to form the English letters “SHU” as shown in Figure 2j. On the macro scale, we prepared two-dimensional codes on transparent and flexible *indium tin oxide* coated polyethylene terephthalate (PET-ITO) substrates as examples (shown in Figure 2m). The bright fluorescence could be seen under excitation with UV light. The link for the two-dimensional code is “http://en.shu.edu.cn”. As shown in Figure S7, compared with the transmittance of the PET-ITO substrate not coated with $CsPbBr_3$, the transmittance of the PET-ITO substrate after coating was only slightly lower (within 10%). These patterns were nearly transparent, which further supports broad applications of our method in anti-counterfeiting. When PET-ITO was processed, only 50 kHz/1.1 W was needed to obtain the desired engraving effect.

Compared with the previous perovskite patterning techniques[35], such as lithography, inkjet printing, laser processing, etc., our method can take advantages of both template-free preparation in full-wafer scale and low consumption of reagents. Only 10 μl of precursor solution was needed to prepare 40,000 droplet arrays in one processing round (Figure S8) of about 30s, and the cost was only 0.0085 USD. The cost of one anti-counterfeiting label containing 1000 PUF patterns is 2.1×10^{-4} USD. (These calculations are detailed in Note S1 of the supplementary materials.)

2.2 Anti-counterfeiting label

2.2.1 Fluorescent patterns with clonable shapes and unclonable texture

A PUF is a physical object with an intrinsic, unique, fingerprint-like feature. Its uniqueness is provided by a random pattern that is based on the random disorder of the microstructure of the object during its manufacturing process; easy to produce but impossible to copy, even by the manufacturer; easy to read but impossible to predict and is unclonable by definition. [5, 7, 36, 37]

Because the nanosecond laser beam has a Gaussian intensity distribution[38], the surface formed by engraving will also show irregular undulations (Figure 1e1, e2). This result has been confirmed by other researchers. [38, 39] The random and uncontrollable crystallization process and the irregular undulations of the engraved surface will also cause the formed crystal film to have a unique texture. In addition, nanosecond laser processing has a thermal effect, which will cause the lyophobic layer outside the predefined pattern to be irregularly damaged to a certain extent, which will eventually cause the formed crystal film edge to be unsmooth (Figure S9). The slightly unsmooth edges will not affect the shape of the formed crystal film but can introduce a unique texture to the outer profile of the crystal film. In short, through this method, we can prepare crystal films with highly similar shapes as shown by Table 1, but each crystal film has a texture of PUF characteristics. These textures are essentially derived from the hierarchical micro-nano structures randomly assembled by nanocrystals. Its manifestation in a fluorescence image is a unique brightness distribution. As shown in Figure 3a3, we used ORB method to extract the texture features which are 2-9 μm.

2.2.2 The shape and texture recognition process

Here, we used nonlearning-based methods for feature extraction, recognition and classification of thin film images. The processing of film pattern recognition and verification is shown in Figure 3 and Figure S10. We used the shape space theory and

an improved method based on Hough circle detection to recognize the shape. If two shapes are matched with the shape space theory method, the numbers of their landmarks need be the same. Then, the smallest geodesic distance between the obser ved shape and the target shape was calculated in the shape space. Here, the number of landmarks on a shape was predefined as p, and the landmarks were represented as $\tau_1=\{\tau_{i1},\tau_{i2},\dots,\tau_{ip}\}$. The distance d_p between the two shapes τ_1 and τ_2 can be calculated using the following equation:

$$d_p\big(O(\tau_1),O(\tau_2)\big)=cos^{-1}\left(\left|\sum_{j=1}^{p}\tau_{1j}\tau_{2j}^{*}\right|\right), \qquad (1)$$

where τ_{1j} and τ_{2j} are the j^{th} complex coordinates of τ_1 and τ_2, respectively, and τ_{2j}^{*} is the complex conjugate of τ_2. This function metric is the well-known Fubini-Study metric, and it is not affected by the distance within the orbitals of the two pre-shaped spaces $O(\tau_1)$ and $O(\tau_2)$. In this way, we can achieve the goal of shape detection and recognition by judging whether d_p between two shapes is small enough.

The shape space theory can find the corresponding feature points on two shapes. However, when the shape are circles, it will be difficult to determine the corresponding relationship between the two circles with the shape space theory. Since circle is the most common shape of the film pattern, we need to use another method to detect a circular shape and ignore the information of the feature points on the circle. Here, we improved Hough circle detection[40] to detect the circle. The detailed steps and description can be found in the supplementary materials Figure S11 and Note S2. In terms of texture matching, considering the matching speed and effect, we chose the grid-based motion statistics matching algorithm proposed by Bian et al. [41] The shape detection time (0.006 s) is much shorter than the texture matching time (1.079 s). Therefore, shape detection can greatly accelerate the whole execution speed with the two-step strategy, i.e., divide-and-conquer algorithm.

2.2.3 Overall identification process based-on divide-and-conquer algorithm

In actual applications, anti-counterfeiting labels are produced in large quantities, so only a few examples of data recognition are inadequate. It is necessary to establish a database with thousands of samples to ensure detection reliability. The authentic film pattern data were saved in the designed database, and the test film pattern was verified through point-to-point matching. To reduce the matching time, here, we adopted the two-step strategy, which was divide-and-conquer algorithm. In other words, we first

performed shape matching and then we performed texture matching for the film patterns. Thus, the databases of film patterns mainly included two sub-databases for shapes and textures. The corresponding operation of establishing the database was mainly image preprocessing, shape information extraction, and texture feature extraction.

Image preprocessing modified the original image by using mathematical and morphological methods. First, the image was subjected to multiple expansion and erosion to obtain a binary image. Due to the randomness of crystal film texture formation, there are relatively large dark spots in some images eventually. We used the hole filling method[42] to fill some of the holes in the image. The minimum outer circle of the pattern was obtained to locate the pattern, and noise shapes were removed by comparing their areas. Finally, the image of the single pattern was normalized. The detailed procedure can be found in the supplementary material Figure S12.

The process of extracting and storing shape information and texture features is shown in Figure S13. The shape information can be described by the landmarks, which were extracted with the method in our previous paper. [43, 44] These points were concentrated in the corners of the shape and accurately reflected the shape, which were stored in the shape database. There are many mature methods for feature extraction, such as SIFT [45], SURF [46], ORB [47], and CNN [48]. We used the ORB method here, and the extracted texture feature points contained the brightness change and neighborhood information of the image since the method ran fast. Additionally, feature description was carried out through binary feature descriptors, and the impact of noise and image scaling change was reduced, while the recognition was accelerated. These types of texture feature data were saved into three files sequentially arranged in the texture database: the film pattern image, the feature geometrical information, and the feature descriptor information. The film pattern image was used to display the image in the interface; the feature geometrical information file saved the information of the feature point to find the location of the feature point; the feature descriptor information file was specifically used for texture matching.

The overall processing flow of our ShaptexMatch technology is shown in Figure 4a. We can extract anti-counterfeiting information from the products and store it in the database after warehousing operations. The user takes images with a portable microscope and a mobile phone and uploads to database. The anti-counterfeiting film pattern information is extracted by the two-step verification of the shape and texture. If

the corresponding anti-counterfeiting pattern is found in the database, then the image is authentic; if no matching data are found, the image is fake.

To increase matching speed, we set the feature points extracted by the algorithm and reduced the number of feature points to 1500 by selecting the maximum Harris response value. To obtain the best matching threshold, we tested multiple matching thresholds to conduct experiments. 47 authentic images and 27 fake images were tested, and the result is shown in Figure 4b. We found that when the feature point matching threshold was set to be 200, the validation accuracy of true images reached 97.9% and the validation accuracy of false images reached 100 %. In other words, we have 2.1% of false negatives and 0% false positives. The authentic film pattern could be found from the database, and the counterfeit pattern could be correctly identified.

In terms of shape category setting, we collected 4000 images to the database and set up seven groups of matching experiments based on the number of the shape classes. These seven groups included no classification, 11 classes, 21 classes, 31 classes, 41 classes, 51 classes, and the current 61 classes. These 61 types of graphics include 60 kinds of circular, pentagonal and other shapes. For specific shape examples, please refer to Figure S14. The 61st type of graphics is the image that cannot be recognized due to the large defects in the above-mentioned shapes (as shown in Figure S15) and complex contours as shown in Figure 3. We developed ShatexMatch authentication software and ran the authentication of 14 patterns (Table S1). The detection costs include the time of the shape detection and the texture detection. The authentic examples are generally stored in the texture library of the corresponding shape. The shape detection was used to narrow the range so that only the texture library of the current shape needs to be traversed during the texture detection. However, the matching of a counterfeit sample was performed after the preliminary shape screening was completed. In addition to traversing all textures under the current shape, it was necessary to traverse in the "complex-shape library". If no matched graphics for the observed film pattern were found, the pattern was not considered in the database. The average counterfeit sample matching time was twice as long as the average matching time for authentic samples. The average matching time is shown in Figure 4c. More detailed matching time can be seen in supplementary materials Table S1. After shape detection, to quickly find the location of the texture library where the film pattern to be matched was located, we predetermined the mapping relationship of the shape texture library when constructing the shape library and the texture library. The averaging matching time was shortened

from 54.18 s to 2.69 s, indicating that the use of specificators can greatly raise the nonlearning-based matching speed over 20 times. The overall processing time is only 12.17s (as shown in Video S1). Deep learning needs to gain more in-depth knowledge when processing multicategory images, so the model needs to be continuously deepened, which leads to more and more complex model structures. Networks such as Alexnet [48], VGG [49], and Resnet [50] have over ten million parameters. We could use our "divide and conquer" approach to process and used the specificators to pre-classify images. The training and prediction time will be shortened accordingly, so that classification and texture recognition with the divide-and-conquer approach since the shape matching can save a lot of execution time.

At the same time, perovskite is prone to failure in a humid environment, which has limited the application potential of perovskite. [51-53] After being spin-coated on the prepared substrate, the polydimethylsiloxane (PDMS) prepolymer was heated and cured to serve as a protective layer for the perovskite. A substrate with a PDMS protective layer and a substrate without a PDMS protective layer were placed in the same environment at the same time (approximately 20°C, 40-60% relative humidity). One month later, the perovskite without the protective layer showed signs of degradation, such as considerably changed color and texture (Figure S16). The sample with the PDMS protective layer had no distinct changes after 60 days and passed our anti-counterfeiting verification, and the matching threshold stayed above 200. The corresponding images and matching data are shown in Figure S17 and Figure S18 Therefore, we believe that the PDMS protective layer can protect the perovskite to a certain extent. Similarly, in order to test the light stability of the prepared label, we irradiated the label with blue light with the intensity of 1.7×10^5 mW/cm^2 and the wavelength of 400-480nm for 1 hour and took photos every 10 minutes. In order to test the temperature stability of the prepared label, we put the label on a hot plate at 80℃ for 1 hour and take photos every 10 minutes. The sample passed our anti-counterfeiting verification, and the matching threshold stayed above 200. Matching data are shown in Figure S19. This has great significance to the real-world application of our anti-counterfeiting labels, but more robust passivation[53-55], such as silica coating[56]and long-chain amine functionalization[57], could be adopted for more humid environment.

The texture feature points of the anti-counterfeiting image were caused by the brightness of the green channel. This brightness value was in the range of 0-255. The image was converted to a size of 960 × 960 during normalization, so there were $256^{960\times960}$ permutations and combinations for an anti-counterfeiting pattern, and the theoretical encoding capacity reached $1\times10^{2,219,212}$ (we referred to the calculation proposed by Jing et al.[16]). According to the Carro-Temboury et al.[58], the effective encoding capacity of film pattern can reached 2.1×10^{623}. (These calculations are detailed in Note S3 of the supplementary materials.) To compare our ShatexMatch technology with other reported PUF anti-counterfeiting technologies, we listed the main parameters in Table 2. As shown in Table 2, our work has the advantages of huge coding capacity, low cost, convenient and fast verification operation. Meanwhile, we summarized the production process of anti-counterfeit label in Figure S21 and showed the verification of anti-counterfeiting label by a portal microscope (Figure S22) in seconds (Video S1). These characteristics have demonstrated the potential application of our anti-counterfeiting system.

3. Conclusions

In summary, by adjusting the temperature and lyophilic region for evaporation-induced self-assembly, we fabricated perovskite nano-crystal film anti-counterfeiting labels with diversified patterns. The film patterns showed high tunability from shape to inner part and from the microscale to the macroscale, high-throughput preparation could be achieved at low cost, and each thin film had a unique texture. At the same time, we established a set of matching recognition algorithms. The data could be refined and classified by changing the shape of the film, and the refining classification could accelerate the recognition speed. It only took a few seconds to complete the authentication. The user only needs a portable microscope with UV light and a smart phone to complete the verification, so no expensive equipment or professional training is needed. Combined the low cost (2.1×10^{-4} USD), convenient and fast authentication (12.17s) and large encoding capacity (2.1×10^{623}), our ShatexMatch technology shows outstanding overall performance.

Since our pattern preparation technique can produce diverse inner and outer profiles, we can extract more feature points on the image profile and incorporate the feature information into the shape information to build a larger anti-counterfeiting label

database with more classes to quickly verify unclonable anti-counterfeit labels. This divide-and-conquer strategy should greatly improve the recognition efficiency regardless of the conventional feature point recognition technique or the bionic deep learning-based recognition technique. In addition, by adjusting the types and proportions of halogens or adapting other type fluorescent dyes, anti-counterfeiting patterns in different colors or components can be easily obtained. Therefore, our advanced evaporative self-assembly technique and authentication strategy show broad applications in micro-nano fabrication and anti-counterfeiting label in the future.

4. Methods

4.1. Substrate preparation

The substrate (such as silicon, *indium tin oxide* (ITO) glass, and PET-ITO) was cleaned with deionized water and dried, and then a plasma cleaner (PDC-002-HP Plasma Cleaner) was used to further clean the substrate. Next, POTS (Sigma-Aldrich, USA) was evaporated and adhered to the substrate, which was placed in an oven at 120°C for 1 hour to obtain a substrate with lyophobic surface. For more detailed steps, see our previous paper. [29-31] The lyophobic substrate was placed into a nanosecond UV laser engraving machine to engrave the surface of the lyophobic substrate, and a substrate with a lyophilic pattern array was obtained. The parameters used in the laser (Bellin SP355-10) were as follows: repetition frequency 50 kHz, average power 1.7 W, and wavelength 355 nm. The obtained substrate was placed in ethanol to conduct ultrasonic cleaning for 5 minutes and then dried to remove spatters generated during engraving.

4.2 Film synthesis

One-step synthesis of perovskite crystal film was achieved by evaporation-induced self-assembly. First, cesium bromide (CsBr, 99.999%, Aladdin Reagent, Shanghai, China) and lead bromide ($PbBr_2$, 99.999%, Aladdin Reagent, Shanghai, China) were dissolved in dimethyl sulfoxide (99.9%, Aladdin Reagent, Shanghai, China) at a molar ratio of 2:1, and ultrasonically assisted dissolution was performed for 4 hours to prepare a precursor solution containing 0.1 M $CsPbBr_3$. As a result, a CsBr-rich solution was formed. Next, in a stable environment (relative humidity less than 30%) inside the glovebox, through a home-made coating device (more details could be found in our previous paper[31]), 10 μL of $CsPbBr_3$ precursor solution with a concentration of 0.1 M was split into tens of thousands of independent precursor droplets and fixed on a specific lyophilic region. The coating process was carried out on a cold plate at 14°C,

and then the substrate was placed on a heating plate at different temperatures for evaporation and crystallization. The anti-counterfeiting label substrate was annealed in a vacuum oven (BluePard DZF-6050) at 80°C for 24 hours, and then a layer of PDMS (Sylgard 184 Silicone Elastomer, Dow Corning Corp, USA) was coated by a spin coater (Setcas KW-4B) at 4000 rpm and solidified in an oven with 60°C. PDMS was purchased as two-part liquid component kits, i.e., base polymer and curing agent.

4.3 Characterization

An optical microscope (Leica DM6 M) was used to view the perovskite film. The fluorescence image of the perovskite film was viewed under an Olympus microscope (IX73, Olympus) at the excitation wavelength of 400-480 nm. An XRD diffractometer (PANalytical Empyrean Alpha 1) was used to measure the perovskite sample (test conditions: CuKα radiation, 40 kV, 40 mA, $\lambda = 1.5406$ Å, $2\theta = 10°-40°$). SEM (Hitachi, SU-8220) was used to measure the thin film sample after evaporation and crystallization at 60°C. The surface profile of the sample was measured with a surface stylus profiler (Alpha-Step D-300). An Edinburgh FS-5 UK fluorescence spectrometer was used to acquire fluorescence spectra. A UV–visible–near-infrared (UV/Vis/NIR) spectrophotometer (PERKIN-ELMER Lambda750) was used to obtain the UV–Vis absorption spectrum and transmittance curve. An Edinburgh Photonics Mini-Tau time-resolved fluorometer was applied to measure fluorescence lifetime at the excitation wavelength of 365 nm using the time-correlated single photon counting technique. The Edinburgh FS-5 UK fluorescence spectrometer was used to measure the PLQY of film via the absolute method.

4.4 Verification of anti-counterfeiting label

A smartphone (model Huawei Mate 30 5G) and an assembled portable microscope (shown in Figure S22) were used to demonstrate the verification process at the end users. 4000 samples were recorded for the database by home-made microscope (shown in Figure S23) with a smartphone (model Huawei Mate 30 5G), a mini-microscope, and a X-Y-Z stage (a part of Leica DM6 M microscope).

4.5 Production process of anti-counterfeit label

We summarized the production process of anti-counterfeit label into six parts: 1. Substrate selection; 2. Using POTS to modify the substrate; 3. Engraving the substrate; 4. Coating; 5. Packaging the label; 6. Attaching the label to the product. The picture of each part is shown in Figure S21.

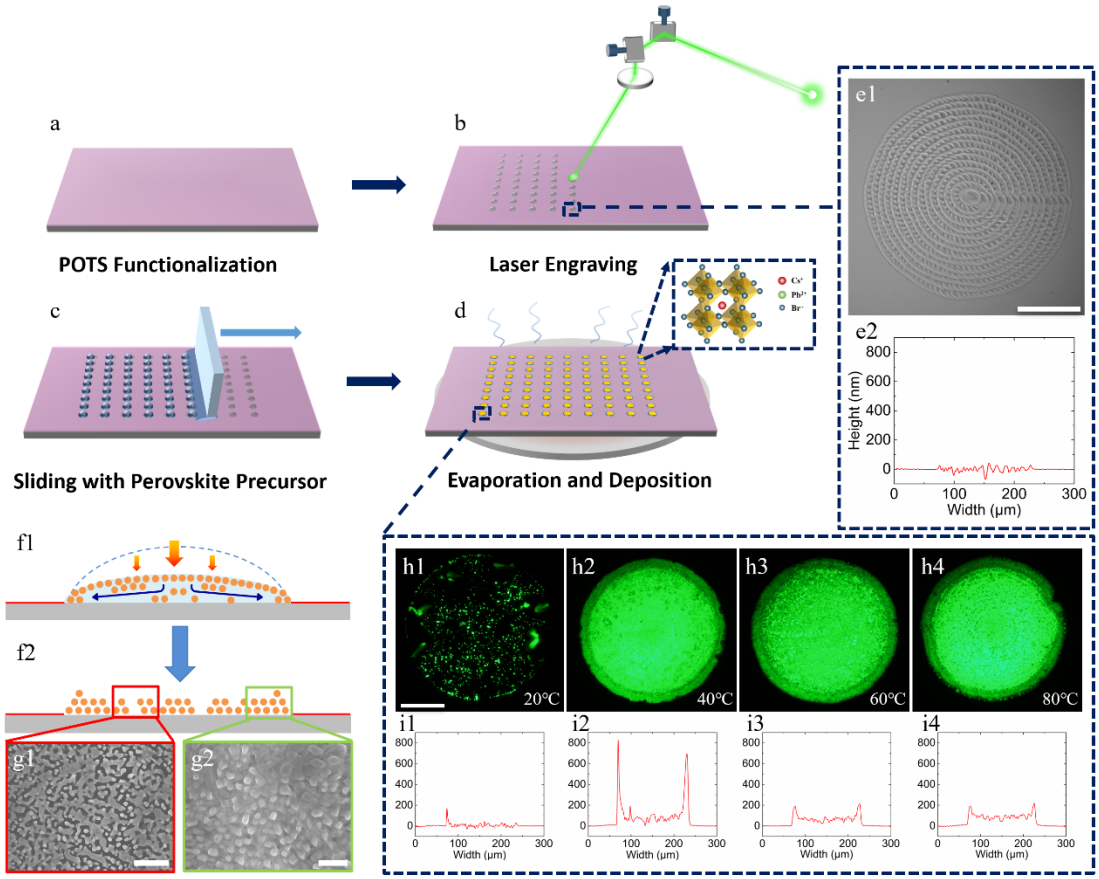

Figure 1. Schematic diagram of using the STC technique to prepare patterned perovskite films. (a) Using POTS to modify the substrate to produce a lyophobic surface. (b) Using a laser to engrave the lyophobic surface to obtain patterned lyophilic regions. (c) Preparing a droplet array with a homemade coating device. (d) Quickly transferring the substrate to the heating plate to accelerate the evaporation of the solvent to form perovskite films. (e) scanning electron microscope (SEM) image after engraving of the hydrophilic pattern (e1) and its corresponding result measured with the profiler. The scale bar in e1 is 50 μm. (f) Schematic diagram of a perovskite film by evaporative assembly. (g) SEM image of a perovskite film. g1 is the enlarged view of the center, and the scale bar is 2 μm; g2 is the enlarged view of the edge part, and the scale bar is 1 μm. (h) the fluorescence images of the perovskite film arrays prepared with the e1 pattern at different temperatures. The scale bar is 50 μm.（i）Results of samples in (h) measured with the profiler.

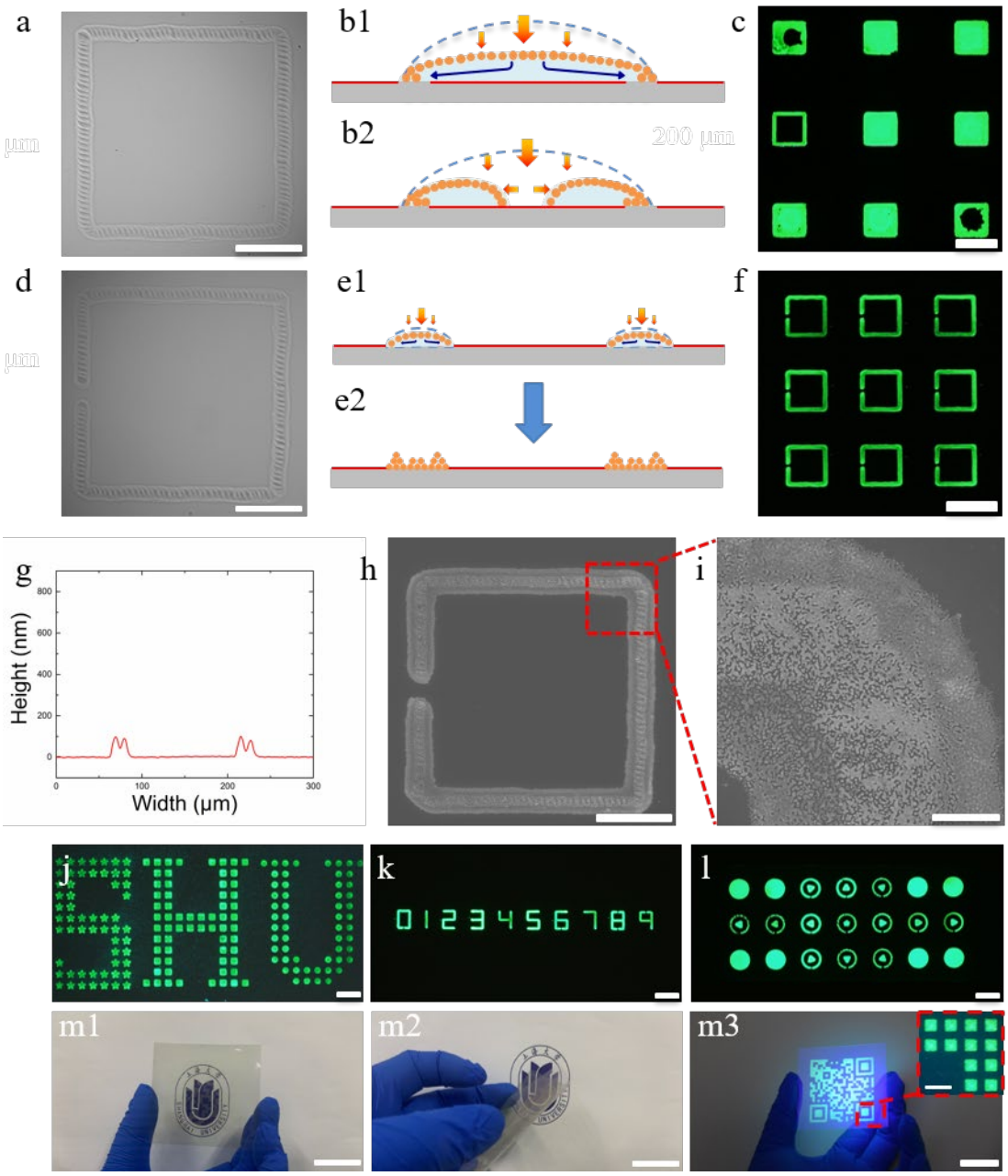

Figure 2. (a) A lyophilic loop pattern. The scale bar is 50 μm. (b) A schematic diagram of the two heating and evaporation modes of droplets corresponding to (a). (c) The fluorescence image of the film corresponding to droplet evaporation in (b). The scale bar is 200 μm. (d) A lyophilic loop pattern with a 14-μm gap. The scale bar is 50 μm. (e) A schematic diagram of the heating and evaporation of the droplet corresponding to (d). (f) Fluorescence image of droplet corresponding to (d) after evaporation. The scale bar is 200 μm. (g) The profilometry result of the circular film in (f). (h) and (i) are SEM images of (f). The scale bars are 50 μm and 5 μm, respectively. (j) The letters "SHU" composed of the thin films of different shapes. (k) Thin films of numbers. (l) A circular film array with an internal pattern and a solid film array using one-step method. (m)

Fluorescent two-dimensional code array prepared on transparent PET-ITO. The scale bar is 3 cm, and the scale bar of the inset is 200 μm.

Type	Tetragon	Pentagon	Hexagon	Heptagon	Octagon	Polygon ...	Complex contours
Examples	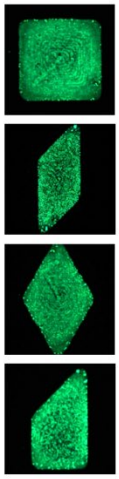	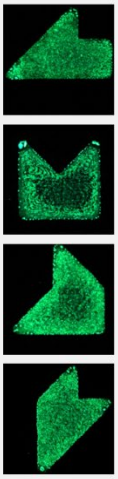	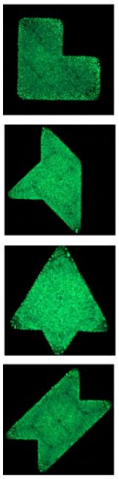	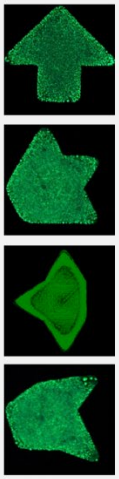	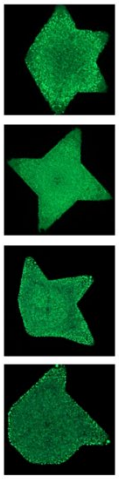		

Table 1. Examples of perovskite crystal films with different contours

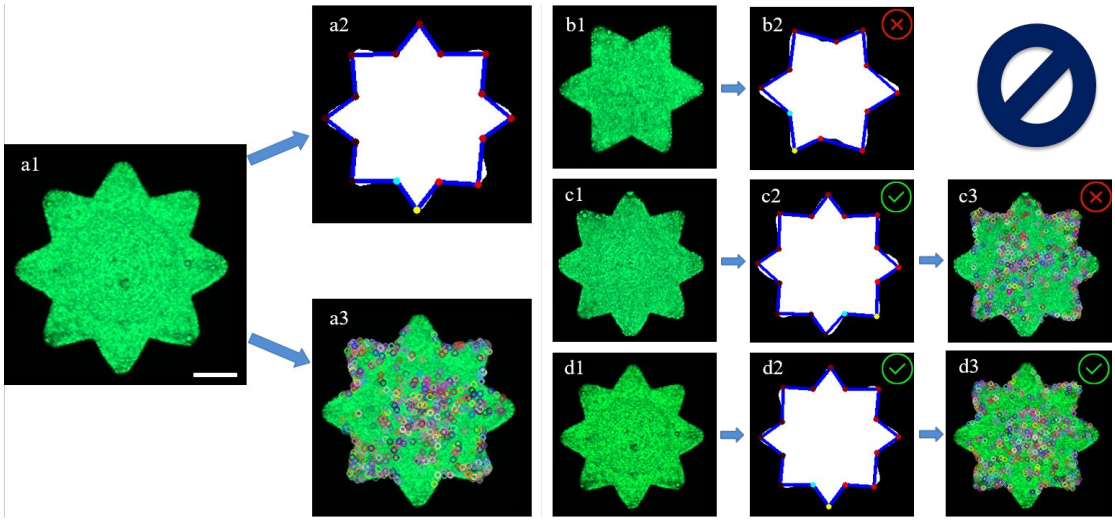

Figure 3. (a) a1 is a perovskite film fluorescence image containing anti-counterfeiting information. The scale bar is 50 μm; a2 is the clonable shape information extracted from a1; a3 is the unclonable texture information extracted from a1. (b) A fake example cannot be verified by shape. (c) A fake example can be verified by shape but not by texture. (d) An authentic image that can be verified both by shape and texture.

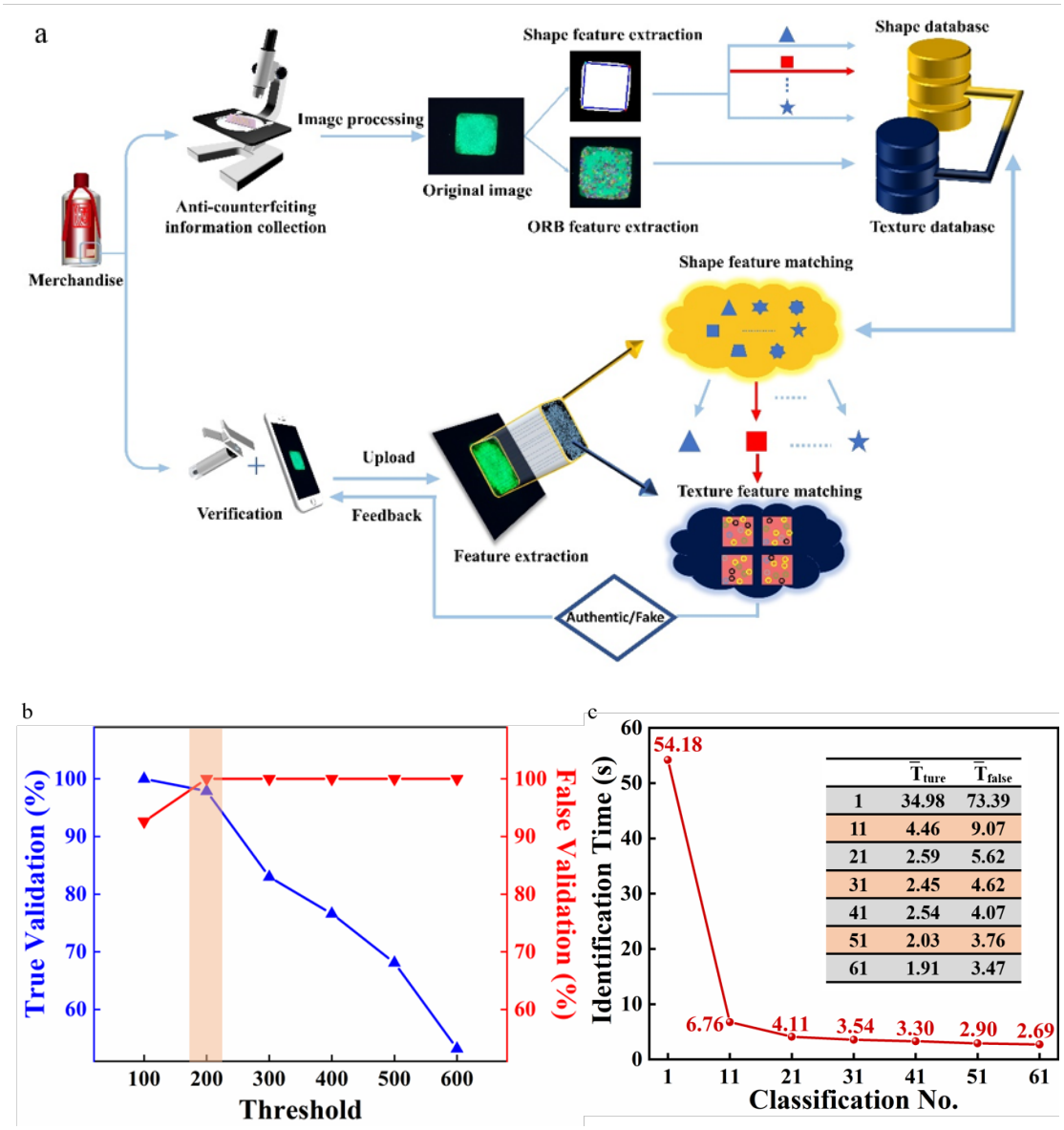

Figure 4. (a) Overall flow chart of the ShetexMatch anti-counterfeiting technology. After the manufacturer constructs the shape database and texture database of the anti-counterfeiting labels, the anti-counterfeiting labels are embedded into the corresponding products. The user only uses a mobile phone and a portable microscope to take the images, which are uploaded to the database for authenticity verification. The authenticity of the product can be verified by matching the shapes and the textures. (b) the validation success rate with different feature point matching thresholds. (c) is the identification time base-on the number of classifications at a threshold of 200. The inset table lists the average matching times for true and false samples, respectively.

PUF type	Authentication device	Encoding capacity	Processing time (Database size)	Reagent cost (USD)	Reference
Polymer wrinkle	Portable microscope +smartphone	1×10^{135}	~40min (1300 samples)	Not available	8, 16
Surface diffuse laser scattering	Laser + photodetectors at different angles	$\sim1\times10^{100}$	~2min (Not available)	Not available	16, 59
Lanthanide dopants	Scanning confocal microscopy	6×10^{104}	~5min (Not available)	Not available	16, 58
Drop-casting gap-enhanced Raman tag	Confocal Raman system	$3\times10^{15,051}$	~20min (100 samples)	Not available	16, 20
Inkjet-printed flower-like pattern	Portable microscope +smartphone	4.7×10^{202}	Seconds ~ minutes (Not available)	2×10^{-3}	11, 16
Crumpling of 2D Materials	Scanning electron microscope	$1\times10^{144,494}$	~3.5 min (1760 samples)	1.6×10^{-3}~2.0×10^{-3}	16
Shaped perovskite fluorescent pattern	**Portable microscope + smartphone**	**2.1×10^{623}**	**12.17s (4000 samples)**	**2.1×10^{-4}**	**This work**

Table 2. Comparisons of main parameters among reported PUF anti-counterfeiting labels.[8, 11, 16, 20, 58, 59]

Supporting Information

Supporting Information is available from the Wiley Online Library or from the author.

Code availability

Computer code used for building the database and validating the data is available in OPENCV algorithm library. The GMS algorithm can be assessed at https://github.com/JiawangBian/GMS-Feature-Matcher.

Author contributions

Y.H.L., H.K.Z, and J.Y.F. contributed equally to this work. J.B.W. conceived the project. Y.X.H. and J.B.W. designed the computer authentication. J.B.W. and Y.H.L. designed the experiments and fabricated the devices. J.B.W. Y.H.L. and J.Y.F. collected the data. J. B.W., Y.X.H., Y.H.L., J.Y.F. and H.K.Z. analyzed the data. J.B.W., Y.H.L., J.Y.F. and B.R.S. assisted sample characterization and data analysis. Y.X.H. and H.K.Z built the authentication database, designed the matching algorithm and wrote the code of the computer authentication. J.B.W., Y.H.L., J.Y.F., Y.X.H, H.K.Z. and Y.B.Q. wrote the

manuscript. J.B.W., T.Y.Z., W.J.W. and Y.X.H. supervised the project. All the authors read and commented on the paper.

Notes: The authors declare no competing interests.

Acknowledgements

We acknowledge the generous financial support from the Natural Science Foundation of China (21775101), the Project 111 (D16002) from the State Administration of Foreign Experts Affairs and the Ministry of Education of China, National Key Research and Development Program of China (2020YFB0704503, 2018YFB0704400, 2018YFB0704402) and Natural Science Foundation of Shanghai (20ZR1419000) and the Energy Materials and Surface Sciences Unit of the Okinawa Institute of Science and Technology Graduate University. We acknowledge Prof. Zuankai Wang of City University of Hong Kong for the helpful discussion and suggestion.

References:

1. K. Degardin; Y. Roggo; P. Margot, *J. Pharm. Biomed. Anal.* **2014**, 87, 167.
2. M. Pecht; S. Tiku, *IEEE Spectr.* **2006**, 43, 37.
3. P. Aldhous, *Nature* **2005**, 434, 132.
4. W. Hong; Z. K. Yuan; X. D. Chen, *Small* **2020**, 16, 1907626.
5. R. Arppe; T. J. Sørensen, *Nat. Rev. Chem.* **2017**, 1, 0031.
6. M. Lehtonen, N. Oertel and H. Vogt, *IEEE International Technology Management Conference (ICE)*, Sophia Antipolis, France, **2007**, pp. 1-8.
7. R. Pappu; R. Recht; J. Taylor; N. Gershenfeld, *Science* **2002**, 297, 2026.
8. H. J. Bae; S. Bae; C. Park; S. Han; J. Kim; L. N. Kim; K. Kim; S. H. Song; W. Park; S. Kwon, *Adv. Mater.* **2015**, 27, 2083.
9. M. X. Xie; G. J. Lin; D. T. Ge; L. L. Yang; L. Z. Zhang; J. Yin; X. S. Jiang, *ACS Mater. Lett.* **2019**, 1, 77.
10. Y. Liu; Y. H. Zheng; Y. B. Zhu; F. M. Ma; X. J. Zheng; K. Y. Yang; X. Zheng; Z. W. Xu; S. M. Ju; Y. T. Zheng; T. L. Guo; L. Qian; F. S. Li, *ACS Appl. Mater. Interfaces* **2020**, 12, 39649.
11. Y. Liu; F. Han; F. Li; Y. Zhao; M. Chen; Z. Xu; X. Zheng; H. Hu; J. Yao; T. Guo; W. Lin; Y. Zheng; B. You; P. Liu; Y. Li; L. Qian, *Nat. Commun.* **2019**, 10, 2409.
12. J. Kim; J. M. Yun; J. Jung; H. Song; J. B. Kim; H. Ihee, *Nanotechnology* **2014**, 25, 155303.
13. H. Cheng; Y. Lu; D. Zhu; L. Rosa; F. Han; M. Ma; W. Su; P. S. Francis; Y. Zheng, *Nanoscale* **2020**, 12, 9471.
14. X. He; Y. Gu; B. Yu; Z. Liu; K. Zhu; N. Wu; X. Zhao; Y. Wei; J. Zhou; Y. Song, *J. Mater. Chem. C* **2019**, 7, 14069.

15. J. W. Leem; M. S. Kim; S. H. Choi; S. R. Kim; S. W. Kim; Y. M. Song; R. J. Young; Y. L. Kim, *Nat. Commun.* **2020**, 11, 328.
16. L. Jing; Q. Xie; H. Li; K. Li; H. Yang; P. L. P. Ng; S. Li; Y. Li; E. H. T. Teo; X. Wang; P.-Y. Chen, *Matter* **2020**, 3, 2160.
17. T. Takahashi, Y. Kudo and R. Ishiyama, *2017 Fifteenth IAPR International Conference on Machine Vision Applications (MVA)*, Nagoya, Japan, **2017**, pp. 202-206.
18. B. Wigger; T. Meissner; A. Forste; V. Jetter; A. Zimmermann, *Sci. Rep.* **2018**, 8, 4738.
19. F. Han; Y. Liu; F. Li; Y. Lu; H. Cheng; Y. Lin; T. Zhao; S. H. Ng; U. Bach; Y. Zheng, *J. Mater. Chem. C* **2019**, 7, 13040.
20. Y. Gu; C. He; Y. Zhang; L. Lin; B. D. Thackray; J. Ye, *Nat. Commun.* **2020**, 11, 516.
21. A. Abdollahi; H. Roghani-Mamaqani; B. Razavi; M. Salami-Kalajahi, *ACS Nano* **2020**, 14, 14417.
22. Y. Zhang; R. Huang; H. L. Li; Z. X. Lin; D. J. Hou; Y. Q. Guo; J. Song; C. Song; Z. W. Lin; W. X. Zhang; J. Wang; P. K. Chu; C. Zhu, *Small* **2020**, 16, 2003121.
23. Y. Liu; F. S. Li; L. C. Qiu; K. Y. Yang; Q. Q. Li; X. Zheng; H. L. Hu; T. L. Guo; C. X. Wu; T. W. Kim, *ACS Nano* **2019**, 13, 2042.
24. M. L. Li; T. Tian; Y. J. Zeng; S. Zhu; J. Y. Lu; J. Yang; C. Li; Y. M. Yin; G. XLi, *ACS Appl. Mater. Interfaces* **2020**, 12, 13494.
25. X. Y. Yu; L. Z. Wu; D. Yang; M. H. Cao; X. Fan; H. P. Lin; Q. X. Zhong; Y. Xu; Q. Zhang, *Angew. Chem.-Int. Edit.* **2020**, 59, 14527.
26. D. Y. Zang; S. Tarafdar; Y. Y. Tarasevich; M. D. Choudhury; T. Dutta, *Phys. Rep.-Rev. Sec. Phys. Lett.* **2019**, 804, 1.
27. M. Parsa; S. Harmand; K. Sefiane, *Adv. Colloid Interface Sci.* **2018**, 254, 22.
28. N. D. Patil; P. G. Bange; R. Bhardwaj; A. Sharma, *Langmuir* **2016**, 32, 11958.
29. Y. Lin; Z. Wu; M. Zhang; J. Wu; W. Wen, *Adv. Mater. Interfaces* **2018**, 5, 1800729.
30. H. Du; K. Wang; L. Zhao; C. Xue; M. Zhang; W. Wen; G. Xing; J. Wu, *ACS Appl. Mater. Interfaces* **2020**, 12, 2662.
31. Y. Y. Lin; Z. S. Wu; Y. B. Gao; J. B. Wu; W. J. Wen, *Appl. Surf. Sci.* **2018**, 442, 189.
32. H. Lama; D. K. Satapathy; M. G. Basavaraj, *Langmuir* **2020**, 36, 4737.
33. Y. N. Li; Q. Yang; M. Z. Li; Y. L. Song, *Sci. Rep.* **2016**, 6, 24628.
34. H. Li; W. Fang; Z. Zhao; A. Li; Z. Li; M. Li; Q. Li; X. Feng; Y. Song, *Angew. Chem. Int. Ed. Engl.* **2020**, 59, 10535.
35. X. Huang; X. Xiao; G. Dong, *Adv. Mater. Technol.* **2020**, 5, 2000513.
36. C. Herder; M.-D. Yu; F. Koushanfar; S. Devadas, *Proc. IEEE* **2014**, 102, 1126.
37. Y. Geng; J. Noh; I. Drevensek-Olenik; R. Rupp; G. Lenzini; J. P. F. Lagerwall, *Sci. Rep.* **2016**, 6, 26840.
38. Y. K. Cai; W. L. Chang; X. Luo; A. M. L. Sousa; K. H. A. Lau; Y. Qin, *Precis. Eng.-J. Int. Soc. Precis. Eng. Nanotechnol.* **2018**, 52, 266.
39. M. E. Shaheen; J. E. Gagnon; B. J. Fryer, *Opt. Lasers Eng.* **2019**, 119, 18.
40. R. O. Duda; P. E. Hart, *Commun. ACM* **1972**, 15, 11.
41. J. W. Bian; W. Y. Lin; Y. Liu; L. Zhang; S. K. Yeung; M. M. Cheng; I. Reid, *Int. J. Comput. Vis.* **2020**, 128, 1580.
42. R. C. Gonzalez; R. E. Woods; B. R. Masters, *J. Biomed. Opt.* **2009**, 14, 029901.
43. Y. X. Han; B. Wang; M. Idesawa; H. Shimai, *Pattern Recogn.* **2010**, 43, 1467.

44. Y. X. Han; H. Koike; M. Idesawa, *Pattern Anal Appl* **2014**, 17, 195.
45. D. G. Lowe, *Int. J. Comput. Vis.* **2004**, 60, 91.
46. H. Bay; A. Ess; T. Tuytelaars; L. Van Gool, *Comput. Vis. Image Underst.* **2008**, 110, 346.
47. E. Rublee, V. Rabaud, K. Konolige and G. Bradski, *2011 International Conference on Computer Vision*, Barcelona, Spain, **2011**, pp. 2564-2571.
48. A. Krizhevsky; I. Sutskever; G. E. Hinton, *Commun. ACM* **2017**, 60, 84.
49. K. Simonyan; A. Zisserman, arXiv:1409.1556, v6, submitted: Apr **2015.**
50. K. M. He; X. Y. Zhang; S. Q. Ren; J. Sun, *2016 IEEE Conference on Computer Vision and Pattern Recognition (CVPR)*, Las Vegas, USA, **2016**, pp. 770-778.
51. Z. Zhang; L. Liu; H. Huang; L. Li; Y. Wang; J. Xu; J. Xu, *Appl. Surf. Sci.* **2020**, 526, 146735.
52. S. Park; W. J. Chang; C. W. Lee; S. Park; H.-Y. Ahn; K. T. Nam, *Nat. Energy* **2016**, 2, 16185.
53. Z.-J. Li; E. Hofman; J. Li; A. H. Davis; C.-H. Tung; L.-Z. Wu; W. Zheng, *Adv. Funct. Mater.* **2018**, 28, 1704288.
54. X. Huang; Q. Guo; D. Yang; X. Xiao; X. Liu; Z. Xia; F. Fan; J. Qiu; G. Dong, *Nat. Photonics* **2019**, 14, 82.
55. Y. Wang; J. He; H. Chen; J. Chen; R. Zhu; P. Ma; A. Towers; Y. Lin; A. J. Gesquiere; S. T. Wu; Y. Dong, *Adv. Mater.* **2016**, 28, 10710.
56. C. Sun; Y. Zhang; C. Ruan; C. Yin; X. Wang; Y. Wang; W. W. Yu, *Adv. Mater.* **2016**, 28, 10088.
57. Y. Dong; X. Tang; Z. Zhang; J. Song; T. Niu; D. Shan; H. Zeng, *Matter* **2020**, 3, 273.
58. M. R. Carro-Temboury; R. Arppe; T. Vosch; T. J. Sørensen, *Sci. Adv.* **2018**, 4, e1701384.
59. R. Cowburn, *Contemp. Phys.* **2008**, 49, 331.